INL/EXT-21-63331

Data Analysis of the 2020 Central Idaho Mainshock-Aftershock Sequence

June 2021

The INL is a U.S. Department of Energy National Laboratory
operated by Battelle Energy Alliance

INL/EXT-21-63331

Data Analysis of the 2020 Central Idaho Mainshock-Aftershock Sequence

Lee M. Liberty, T. Dylan Mikesell, and Spencer Wilbur
Boise State University
Department of Geosciences
Boise, Idaho
(Boise State Project #2000001740)

June 2021

Idaho National Laboratory
Idaho Falls, Idaho 83415

http://www.inl.gov

Prepared for the
U.S. Department of Energy
Office of Nuclear Energy
Under DOE Idaho Operations Office
Contract DE-AC07-05ID14517

ABSTRACT

In an effort to inform the Senior Seismic Hazard Analysis Committee (SSHAC) Level 3 project for the Idaho National Laboratory, we provide an improved aftershock catalog related to the March 31, 2020, Mw6.5 Stanley, Idaho earthquake from picks related to a temporary network of two real-time and 15 non-telemetered seismometers within the epicentral area. From the permanent and temporary (XP) real-time network, the USGS cataloged 1,946 aftershocks between April 1, 2020 and October 31, 2020. To improve aftershock location and magnitudes, we manually picked arrival times of P and S waves from off-line stations in the XP temporary network, generated a new crustal velocity model, and independently relocated each event using the HypoDD double-difference earthquake algorithm. We created our new velocity model from existing broadband and active source seismic campaign data that were acquired near the epicentral region prior to the 2020 earthquake. We compare arrival time differences, epicentral locations and depths between aftershocks recorded with the two catalogs. We find the addition of local stations provides tighter aftershock clustering that suggests an improved aftershock locations. To detect lower magnitude events, we employed deep learning. Our method solves common problems associated with detecting many events that have a low signal-to-noise ratio. From the machine learning database, we detected more than 74,000 aftershocks. Based on the number of identified earthquakes and Gutenberg-Richter relationships derived from the USGS catalog, we estimate that we have reduced the completion magnitude for the Stanley earthquake sequence to below M1 using this machine learning approach. We located each aftershock with our new velocity model. Our new velocity model and picks suggests aftershocks occurred mostly at shallower depths than assessed in the USGS catalog. These aftershocks align along two linear trends that suggest the activation of two unnamed primary faults.

Table of Contents

Introduction 1
Catalog #1: USGS real-time database 3
Catalog #2: Temporary network database 4
Catalog #1 and #2 comparisons 6
Seismic Data Collection and Machine Learning: 9
Machine Learning Catalog Construction: 12
Faulting Revealed by Aftershocks 14
Summary 14
References 14

Introduction

The March 31, 2020, M_w6.5 Stanley, Idaho, earthquake was felt throughout the US Pacific Northwest, area. Due to its remote location, only minor structural damage was identified (e.g., Liberty et al., 2021; Pollitz et al., 2021; Yang et al., 2021). Yet, this earthquake is only one of a few in central Idaho that have been instrumentally recorded with a robust local seismic network. Central Idaho is seismically active, and this earthquake sequence has some unknown relationship between the NW-trending Sawtooth fault, the NE-trending Trans-Challis fault system, and possibly other unmapped faults (Figure 1). Understanding fault kinematics and aftershock patterns related to the Stanley earthquake sequence may improve our understanding of fault systems and ground amplifications throughout the region.

As part of new data compilation activities for the Senior Seismic Hazard Analysis Committee (SSHAC) Level 3 project, detailed locations for the Stanley mainshock and aftershocks are needed for input to the project's regional seismicity catalog and other analyses. The SSHAC Level 3 project supported the Boise State team to perform analyses of the Stanley aftershock data that was acquired using permanent telemetered seismic network and a temporary array of 15 stations. Deployment of the temporary array was funded by the US Geological Survey National Earthquake Hazards Program (Liberty and Mikesell, 2021). Here, we focus on the use of the local network to improve aftershock characteristics.

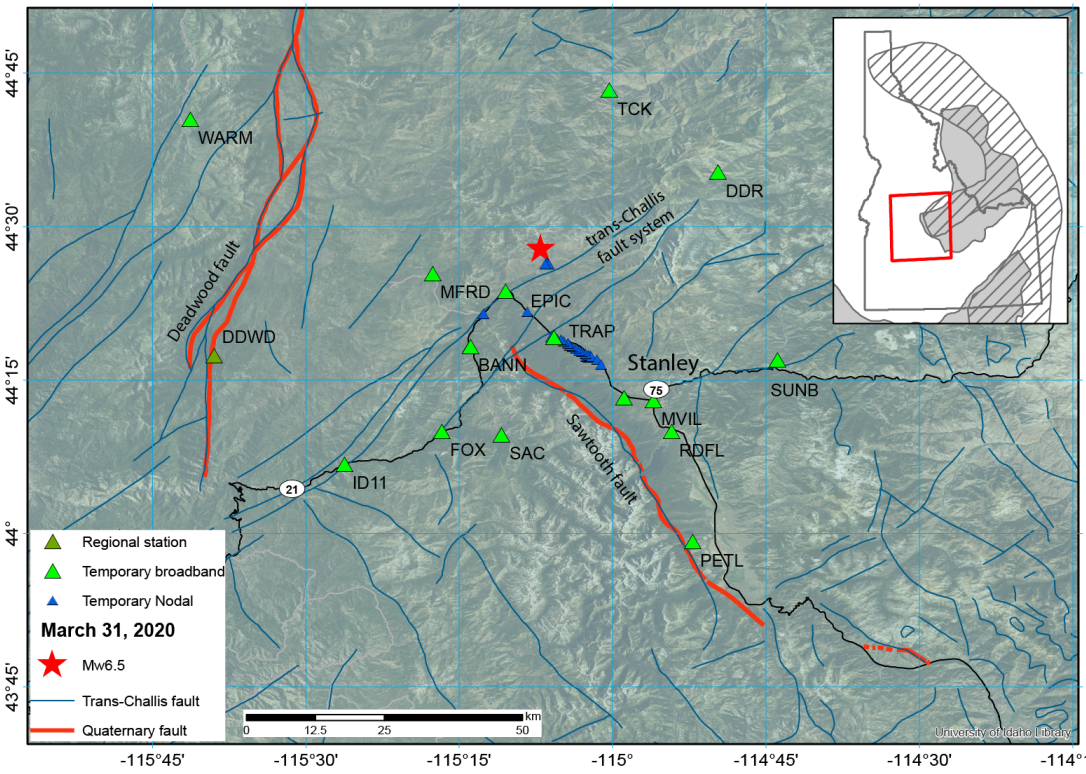

Figure 1. Location map for the Stanley earthquake and the temporary seismic network for central Idaho. The Sawtooth and Deadwood faults are considered late-Quaternary active.

In this report, we describe the creation and significance of three earthquake catalogs that will improve our understanding of active faulting and earthquake hazards for Idaho (Table 1). First, we describe the real-time earthquake catalog derived from hand-picked compression (P) wave and shear (S) wave phases extracted from a permanent telemetered seismic network (U.S. Geological Survey, 2020). We then describe how we generate a second earthquake catalog from these same aftershocks using a double-difference algorithm approach. For this second catalog, we use a similar picking approach as with the USGS real-time catalog, but we add P- and S-phase picks and amplitudes from a local 15-station network (Berti et al., 2020) to compute local magnitudes (M_L) of some events. Additionally, we generate a new, regionally appropriate velocity model from a suite of campaign seismic data that focused on the crustal structure of central Idaho. We describe the velocity model that was derived from previously published studies and how this new velocity model changed our aftershock locations and depths. Finally, we describe a third catalog, based on a machine-learning approach, which substantially increased the number of aftershocks that were similar in waveform character to those events in the hand-picked catalog. This third catalog includes aftershock location and depth estimates, but magnitude estimates for this catalog are not included in this report.

Table 1. Summary of three aftershock catalogs. Catalog #1 is the real-time USGS catalog. Catalog #2 uses the same aftershocks as Catalog #1 with local stations. Catalog #3 uses local station coverage with a machine-learning, automated pick approach.

	Catalog #1 (real-time)	**Catalog #2 (post-processed)**	**Catalog #3 (machine - learning)**
Date Range	03/31/2020 - 10/24/2020	03/31/2020 - 10/24/2020	03/31/2020 - 12/31/2020
Detected Events	1,946	1,995	74,686
Network	USGS	XP/USGS	XP
Velocity Model	AK-135	Updated 1D-Velocity Model	Updated 1D-Velocity Model
Picking	Manual Inspection with Seisan	Manual Inspection with Seisan	EQTransformer
Magnitude	ML	ML, Mw, Mb, Mwr	NA
Amplitude	Wood-Anderson	Wood-Anderson	NA

Catalog #1: USGS real-time database

A network of global seismometers provided real-time earthquake waveforms to the seismology community. From this network, the USGS routinely provides near real-time earthquake characteristics that includes moment magnitude (M_w), epicentral location, and hypocentral depth (U.S. Geological Survey, 2020). Due to the sparse coverage of seismic stations in central Idaho, relatively few aftershocks related to the Stanley earthquake were initially located (Figure 2). The database accuracy and completion threshold is dependent on manual P-wave and S-wave arrival time picks from seismometers at a range of distances. Without near-field station coverage, location uncertainties increase and detailed energy radiation patterns (i.e. moment tensor solutions) that can help determine the direction of fault motion, are difficult to assess. Without local stations, low magnitude aftershocks will be absent from the catalog. Additionally, the real-time catalog relies on the AK135 velocity model (Kennett et al., 1995) that may not be appropriate for all geographic locations.

Although 1,928 earthquakes were included in the USGS catalog between March 31 and October 31, 2020, this catalog produced a relatively high completion magnitude of M2.4 (Liberty et al., 2021). In comparison, the 2014 through 2017 Challis earthquake sequence produced a completion magnitude of M1.8 within the same real-time catalog (Pang et al., 2018). Within hours after the March 31, 2020, M_w6.5 Stanley earthquake, a Boise State team installed two USGS broadband seismometers (ID11 and MVIL) within the epicentral region to improve the real-time coverage related to the aftershock sequence (Figure 1). Although internet coverage was intermittent at these two stations, numerous aftershocks were recorded to provide improved locations with inclusion of only these two stations (M. Stickney, personal comm). We note that without additional stations within central Idaho, future earthquakes will remain poorly characterized.

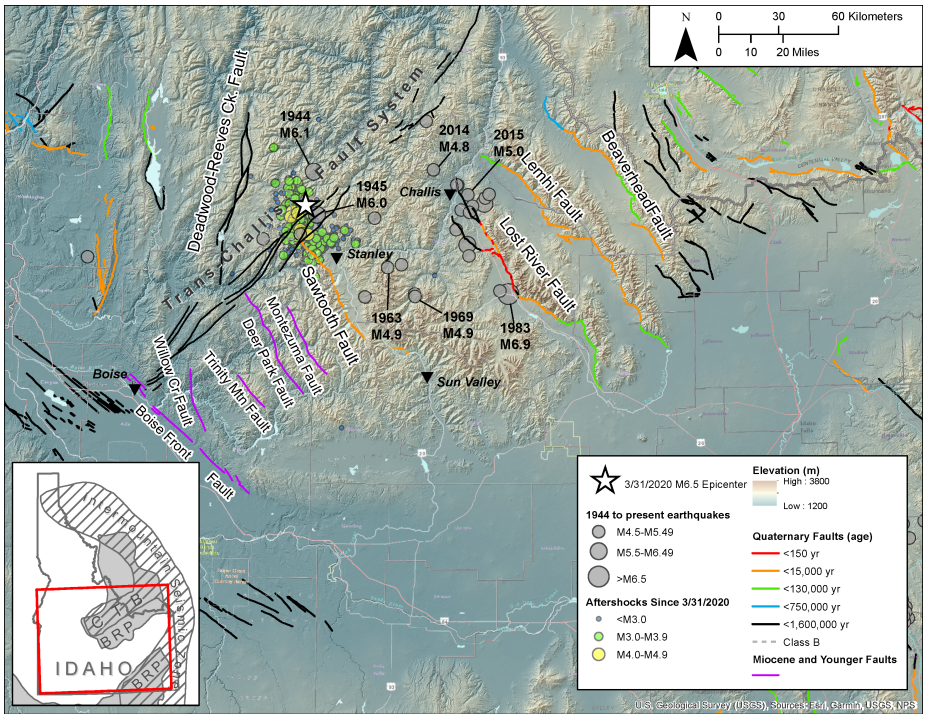

Figure 2. Stanley earthquake aftershocks with other significant earthquakes in central Idaho. Figure from Liberty et al. (2021).

Local velocity model

The Stanley earthquake initiated near the intersection of the Idaho Batholith and Basin and Range Province of central Idaho near the northern termination of the Quaternary NW-trending Sawtooth normal fault at its junction with Eocene NE-trending Trans-Challis fault system (Figure 2; Liberty et al., 2021). Although these two provinces contain different crustal rocks, regional models suggest similar velocities throughout the epicentral region (Stanciu et al., 2016; Davenport et al., 2017; Bremner et al, 2019).

To obtain velocity models for central Idaho, Stanciu et al. (2016) used receiver functions derived from 85 broadband seismic stations to explore the transition from accreted terranes to Proterozoic North American rocks. The receiver function data provide travel time delays between teleseismic P-wave and S-wave arrivals that arrive at near vertical incidence. From these arrivals, depth to key boundaries (e.g., Moho) and Vp/Vs estimates were derived. From active source data, Davenport et al., (2017) explored the same marine/continental crustal transition, but directly estimated Vp through explosive sources deployed along a 430km long refraction and wide-angle-reflection profile. This approach utilized first arrival travel time inversions to derive a best-fit Vp model. This study also identified reflected returns in the middle to lower crust that may be relevant to this study (e.g., brittle-ductile transition). Bremner et al (2019) used the same station array as the Stanciu et al (2016) study, but utilized surface wave information to derive crustal Vs models. We extracted the closest velocity model to the Stanley earthquake location from each of the three studies to derive our local Vp and Vs models (Figure 3). Due to software restrictions, we simplified each velocity model to obtain each of our aftershock location catalogs. This new model was used for aftershock locations to construct our manual and machine-learning catalogs.

When comparing our local velocity model generated from these three regional studies to the AK135 model, we show the depth to the base of the crust is 35 km depth (below sea level) for both models (Figure 3). However, local velocities for the upper 5 km and 20 to 35 km depth are slower by as much as 0.5 km/s. Included in our analysis, we compare depth estimates using both velocity models, but we suggest our local velocity model derived from the 1-D Vp and Vs profiles improves our aftershock locations.

Catalog #2: Temporary network database

To improve aftershock location and magnitude data from the Stanley earthquake, a Boise State team installed an additional 15 seismometers throughout the epicentral region (Figure 1; Table 2; Liberty et al., 2021). Because internet and cellular network coverage was not available, time-series waveforms were recorded to local data loggers and downloaded, on average, once per week. These data were uploaded to the IRIS Data Management Center (Berti et al., 2020; http://www.fdsn.org/networks/detail/XP_2020/) and are publically accessible.

Using the XP network, a team from Boise State (Dr. Dylan Mikesell and Spencer Wilbur), Idaho National Laboratory (INL; Blaine Bockholt), and Montana Bureau of Mines and Geology (Mike Stickney) picked P and S phase arrivals for 1,946 aftershocks through October, 2020 that were identified by the USGS real time catalog. We used SEISAN (Havskov et al., 2020) to interactively pick earthquake phases, Hypoinverse (Klein, 2000) to incorporate the

phase picks with both velocity models to estimate the hypocenter parameters, and HypoDD (Waldhauser and Ellsworth, 2000) to relocate each aftershock.

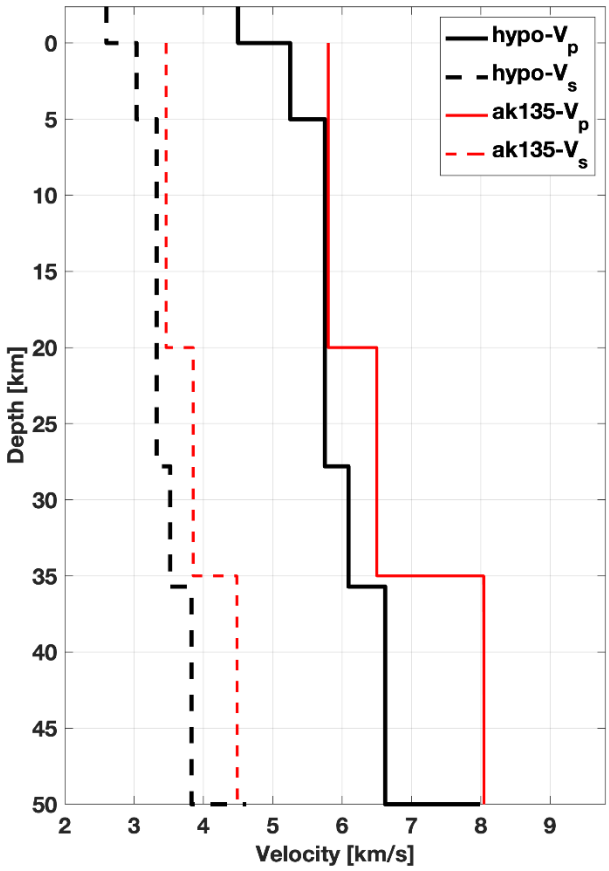

Figure 3: Local velocity model derived from regional seismic surveys (black) and AK135 crustal/mantle velocity model (red) from Kennett et al. (1995). Note that the local velocity model is slower than the AK135 model for all crustal depths. The base of the crust is at 35 km depth below sea level.

The Wood-Anderson amplitudes of both horizontal component channels were picked by the Boise State team for all 248 M>=3 aftershocks. The instrument response of each channel was first removed and the Wood-Anderson response was convolved with the time series to mimic horizontal component Wood-Anderson data. The minimum and maximum amplitudes following the S-wave were then picked. These amplitude data were then used to compute local magnitude (ML) for each event in the catalog with M>=3. The computation was done within SEISAN using the default coefficients of the INL. A few instruments appeared to provide very large ML values and it was determined that these sensors must have an error in their metadata. These stations were ID11, IRON and FOX (Table 2), and it was often that these ML values were an order of magnitude or larger than the other stations in the network. Therefore, the amplitudes on these three stations should be deemed unreliable until the metadata can be corrected and the amplitude picks can be recomputed.

Table 2. Name, location, owner and instrument related to the XP seismic network.

Station	Latitude	Longitude	Elevation (m)	Owner	Instrument
BANN	44.3046	-115.2319	2139.8	BSU	120 s Nanometrics Trillium
EPIC	44.3943	-115.1750	2000.7	BSU	120 s Nanometrics Trillium
TRAP	44.3193	-115.0957	2035.4	BSU	120 s Nanometrics Trillium
IRON	44.2206	-114.9812	1940.8	BSU	120 s Nanometrics Trillium
FOX	44.1661	-115.2781	1482.5	BSU	120 s Nanometrics Trillium
SAC	44.1608	-115.1811	1540.8	BSU	120 s Nanometrics Trillium
MVIL	44.2166	-114.9335	1909.4	IRIS	120 s Meridian Compact Posthole
BSM5	43.5934	-115.9672	946.3	BSU	120 s Nanometrics Trillium
ID11	44.1128	-115.4372	1305.5	USGS	120 s Meridian Compact Posthole
WARM	44.6746	-115.6884	1582.5	IRIS	120 s Meridian Compact Posthole
TCK	44.7219	-115.0056	1343.1	IRIS	120 s Meridian Compact Posthole
DDR	44.5886	-114.8281	1676.9	IRIS	120 s Meridian Compact Posthole
MFRD	44.4236	-115.2939	1950.4	BSU	120 s Nanometrics Trillium
RDFL	44.1656	-114.9043	1981.8	IRIS	120 s Meridian Compact Posthole
PETL	43.9866	-114.8700	2171.8	IRIS	120 s Meridian Compact Posthole
SUNB	44.2827	-114.7313	1841.2	IRIS	120 s Meridian Compact Posthole

Catalog #1 and #2 comparisons

We compare origin time differences in between the USGS catalog #1 and our catalog of aftershocks when we add the temporary network picks (catalog #2). We note that for 1,946 aftershocks identified in catalog #1, we identify travel time differences with respect to distance of generally less than one second (Figure 4). Our analysis shows that catalog #2 records slightly faster arrival times will slightly change aftershock locations and depths. From our assessment, we conclude that arrival times from our XP network can be used for aftershock location and depth estimates.

We next compare the aftershock locations and depths derived from the two catalogs (Figures 5 and 6). Catalog #2 arrival times, coupled with our newly derived local velocity model, results in epicentral location differences upwards of 10 km (Figure 5). The relocations also produced a tighter spatial aftershock cluster that is consistent with motion along only a few fault planes (Figure 7). Depth estimates of the two catalogs varied considerably with the improved travel time and epicentral location database (Figure 7). This is especially true for the aftershocks in the USGS catalog that were assigned a default 10 km depth. We note that we locate the majority of earthquakes at shallower depths when compared to the USGS catalog.

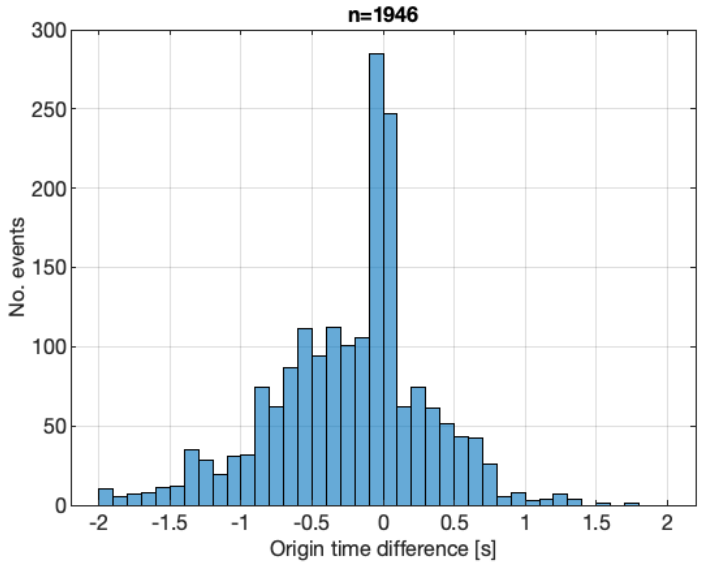

Figure 4. Origin time differences between real-time USGS catalog #1 and the manual picks of catalog #2 from the XP temporary network. Negative origin time implies earlier arrival time for catalog #2.

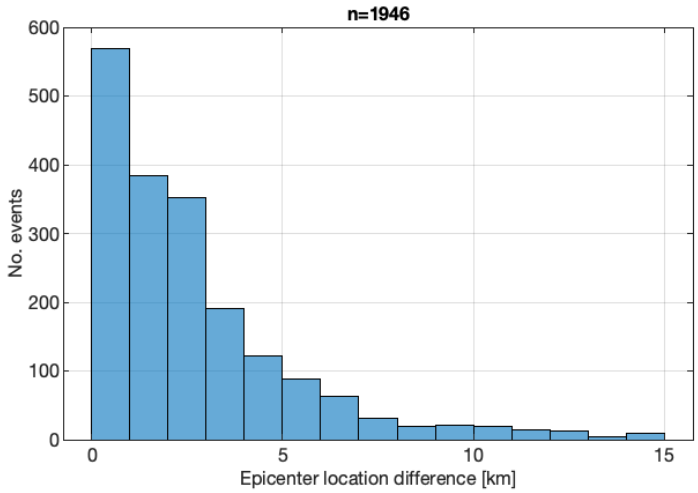

Figure 5. (left) Aftershock location differences between USGS and XP network catalogs. (below). Aftershock differences in latitude and longitude. Note that most of the aftershocks were relocated to the west and south of the USGS catalog.

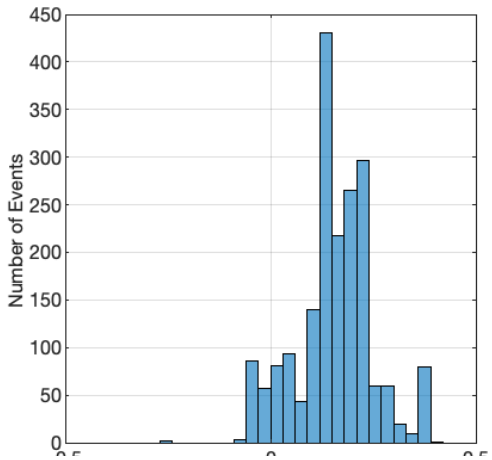

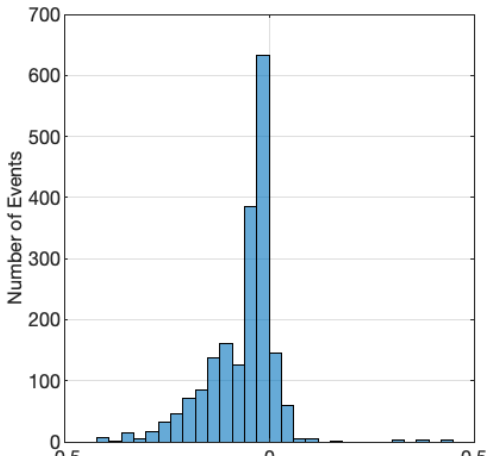

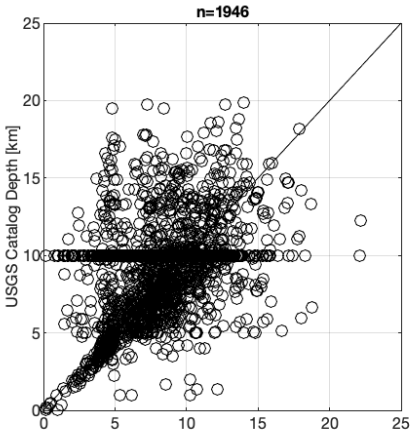

Figure 6: Crossplot of real time network depth estimates to our local station depth estimates. We used HypocenterDD to estimate depths for each aftershock. A 10 km depth represents the default earthquake depth.

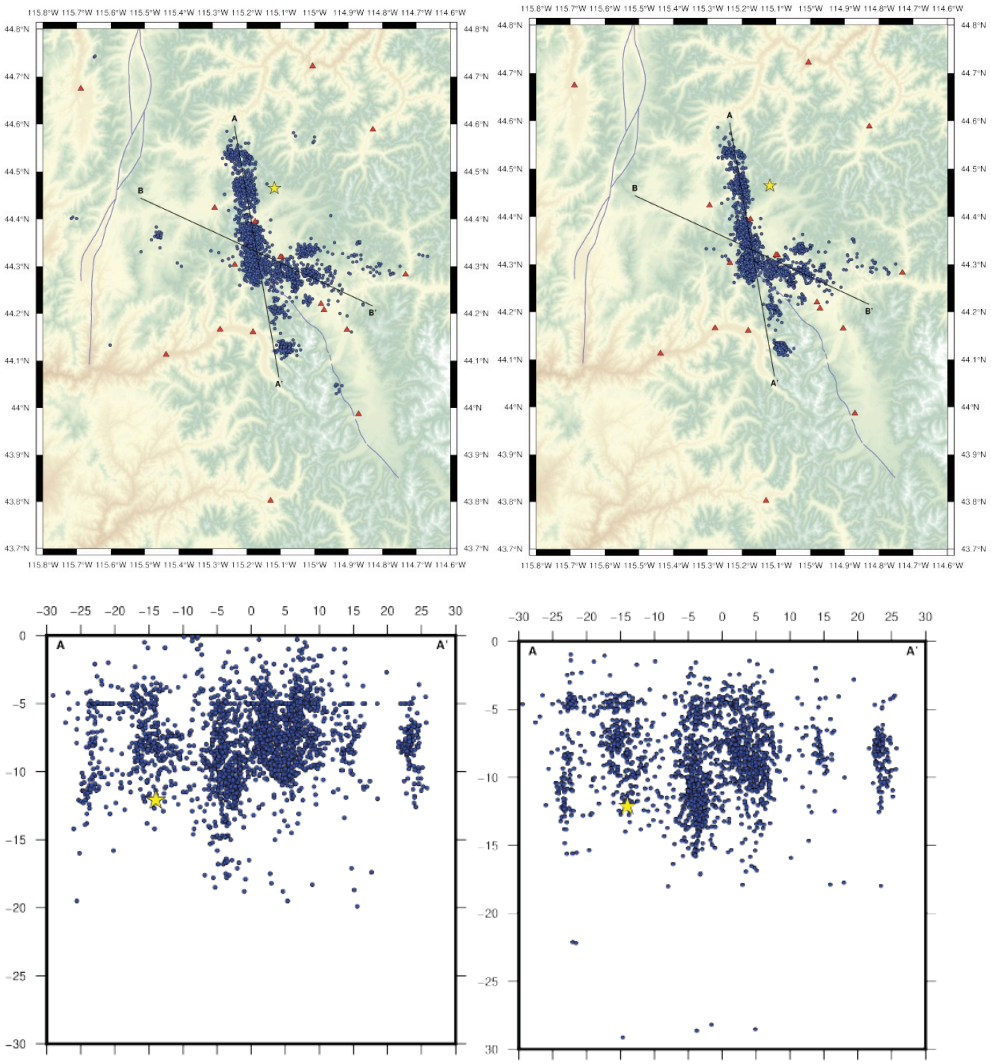

Figure 7. Catalog #1 (top left) and catalog #2 (right) aftershock locations. A-A' cross sections from the two databases (bottom). Figure revised from Bockholt et al. (2021).

To compare differences between the two velocity models, we show that the average depth for all M>3 earthquakes in catalog #1 is 10.4 km with a median depth of 10.0 km (Table 2). Including the picks from the XP network and the AK135 model, we show an average depth of 5.4 km and a median depth of 7.5 km. We attribute the shallower depths to the reduced travel times manually picked with the XP network. When we run this same analysis of XP travel times using our local velocity model, we show an average depth of 8.9 km and a median depth of 5.0 km. We attribute the depth increase when using our local velocity model and the XP network picks to the slower local velocities at shallow depths when compared to the AK135 model (Figure 3). In summary, additional station picks at closer station distances reduces aftershock depths using the global AK135 model. However, using a more appropriate velocity model increased our depth estimates. Given tighter aftershock clustering observed with the XP network and the local velocity model when compared to the USGS catalog (Figure 7), we suggest the inclusion of XP picks and a revised velocity model has improved our aftershock locations.

Table 2. Depth comparisons between Catalog #1 and Catalog #2 using both AK135 and local velocity models.

Catalog	**USGS catalog #1**	**XP catalog #2**	**XP catalog #2**
M>=3	**AK135 velocity model**	**AK135 velocity model**	**local velocity model**
Mean depth (km)	10.4	5.4	8.9
Median depth (km)	10.0	7.5	5.0

Seismic Data Collection and Machine Learning:

Following the completion of manual phase picks using the updated velocity model, we implemented a new neural network approach to generate a more complete aftershock catalog. We used the same aftershock window as with our manual pick database. To assess the quality of the machine learning phase arrivals, we compare them with the manually picked phases using SEISAN. The motivation for an automated approach to earthquake detection and phase picking was that this approach can outperform traditional phase-picking and detection algorithms in the presence of noise and without manual picking biases.

A standard earthquake phase picking method relies on a Short Term Average/Long Term Average (STA/LTA) approach. However, this approach does not perform well when the signal to noise ratio is low. A newer approach is to use an attentive deep learning algorithm that is not as limited by the signal to noise ratio. We selected the EQTransformer detection algorithm (Mosher and Audet, 2020) to locate small magnitude earthquakes. This is a multi-task deep neural network that can be used for simultaneous earthquake detection and phase picking, while also treating each segment of continuous seismic data as a possible template for potential earthquakes (Mousavi & Ellsworth et al., 2020). This approach recognizes similarities in waveforms to an

existing detected earthquake and uses this as a method to detect potential aftershocks. The process for identification can be broken down into two levels of self-attention, a global and local level; each level helps the program capture and exploit dependencies between local (individual phases) and global (full-waveform) features that are emitted from an earthquake signal (Mousavi & Ellsworth et al., 2020). The continuous data being fed to the algorithm are obtained using three-component seismometers.

Using the EQTransformer package, we identified over 74,000 aftershocks. EQTransformer is a deep neural network for simultaneous earthquake detection and phase picking. Using P- and S-wave picks identified for each potential event, EQTransformer also does a simple association, using a station number threshold (e.g. the event must have been observed on N stations). We required that the EQTransformer only associate an event if the event was present on N=6 stations in the temporary network. This is how we arrived at 74,000 potential events. After association, the P and S picks for the potential aftershocks were exported to a Hypoinverse phase file. The events were then located using the same velocity model as the handpicked events and identical Hypoinverse parameters. The resulting ~74,000 aftershocks were then given a grade automatically by Hypoinverse of A, B, C, or D (Figure 8). This grade is related to the residuals of the picks after finding the optimal hypocenter parameters given the EQTransformer picks. The D-grade picks appear to be poorly located and have hypocenters all over the region. A number of these D events do align with the known aftershock structure, but no in-depth investigation has been completed into why some D events might be better than others. The same is true for C grade events. In comparison, A and B grade events have low average residuals and appear to closely follow the known aftershock spatial structure.

Using the hand-picked events, a comparison between P- and S-wave pick differences was performed (Wilbur et al., 2021). On average, EQTransformer picks were within +/- 0.2 s for P and S picks compared to handmade picks. However, the grade of the Hypoinverse solutions have not been studied in detail yet, and we assume that the grade A and B events comprise the majority of the hand-picked events. Future work will investigate the signal-to-noise ratio (SNR) of the waveforms in C and D grade to determine if low SNR is playing a role in the ability of EQTransformer to pick P and S waves accurately.

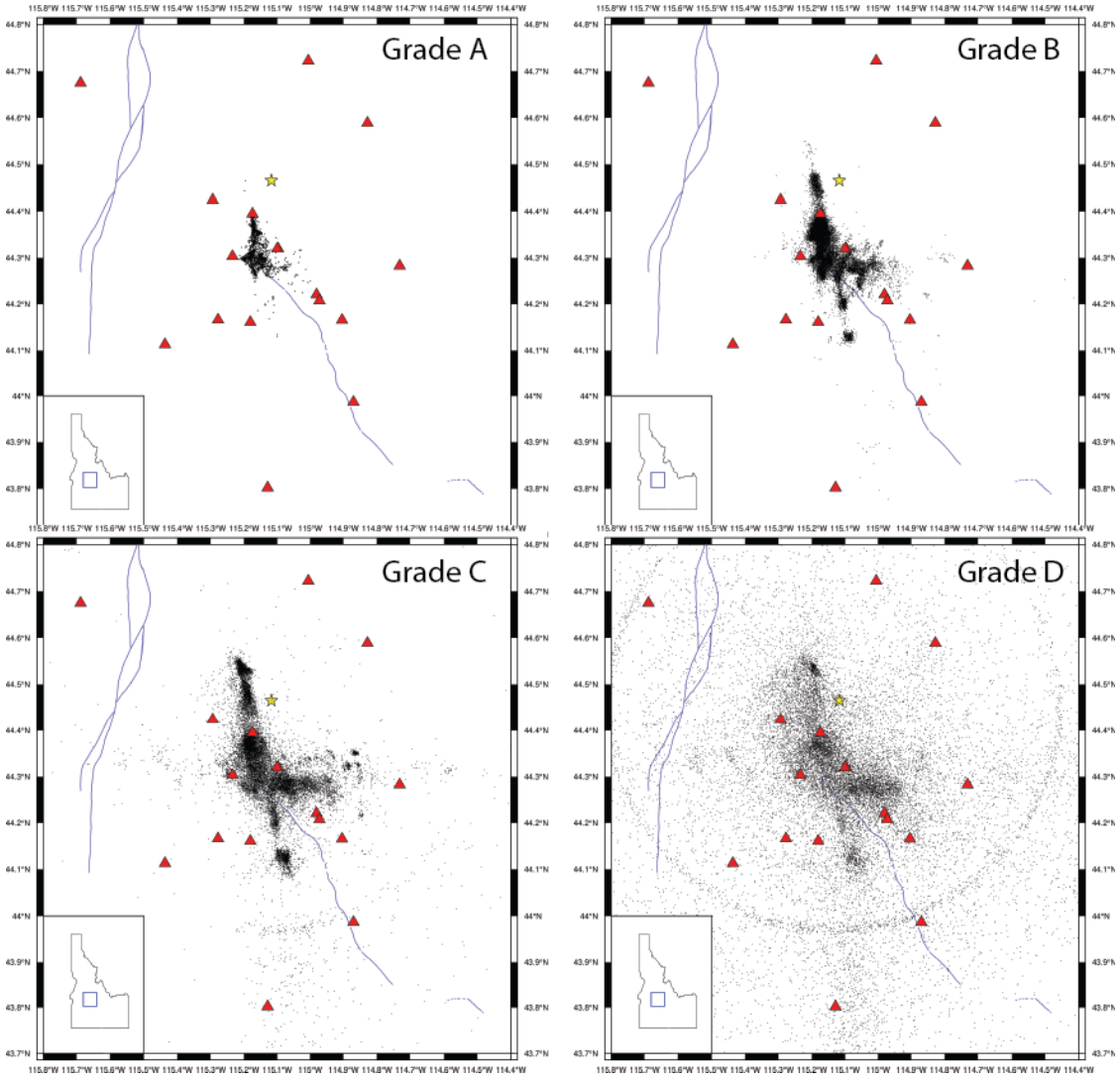

Figure 8. Grade A, B, C and D picks (black dots) derived from Hypoinverse for our machine learning Catalog 3. Red triangles represent XP station network. Blue lines represent mapped faults of the USGS Quaternary fault and fold database (https://usgs.maps.arcgis.com/apps/webappviewer/index.html?id=5a6038b3a1684561a9b0aadf88412fcf).

Machine Learning Catalog Construction:

Once the EQTransformer machine learning algorithm was functioning and providing useful seismic event picks, we assessed the pick quality to our manually picked database. We compared hypocenter depth difference, origin time difference, P-wave arrival time difference, S-wave arrival time difference, and the total number of events detected (Figure 9). The major difference between the machine learning catalog and our SEISAN catalog is that while the manual catalog utilizes an earthquake location method, HypoInverse, the phase picking was still required by hand. The manual wave picking limits the completion magnitude of our catalog when a conservative phase-picking approach is used. The automated detection and simultaneous picking algorithm in the machine learning algorithm eliminates the picking step, saves analysis time, and detects many more earthquakes. There was some location bias for events picked by the machine learning algorithm, likely due to the lack of XP stations north of the epicentral zone or the differences in the velocity models (Figures 1 and 3). By using the EQTransformer deep learning detection method, we increased the third local aftershock catalog for the Stanley Earthquake to more than 74,000 events between March 31 and December 31, 2020 (Figure 9). Based on the number of identified earthquakes and Gutenberg-Richter relationships derived from the USGS catalog, we estimate that we have reduced the completion magnitude for the Stanley earthquake sequence to below M1.

To compare catalog #1 with catalog #3, we compare the P- and S- picked arrival times for overlapping events. We show that phase arrivals are measured almost entirely at less than 0.2s difference, supporting a robust machine learning catalog (Figure 10). Detection of small aftershocks will enable observation of event migration patterns, hypocenter clusters, and help answer outstanding questions regarding the cause of seismic activity in the region. Continued work with this database will allow an in-depth aftershock analysis.

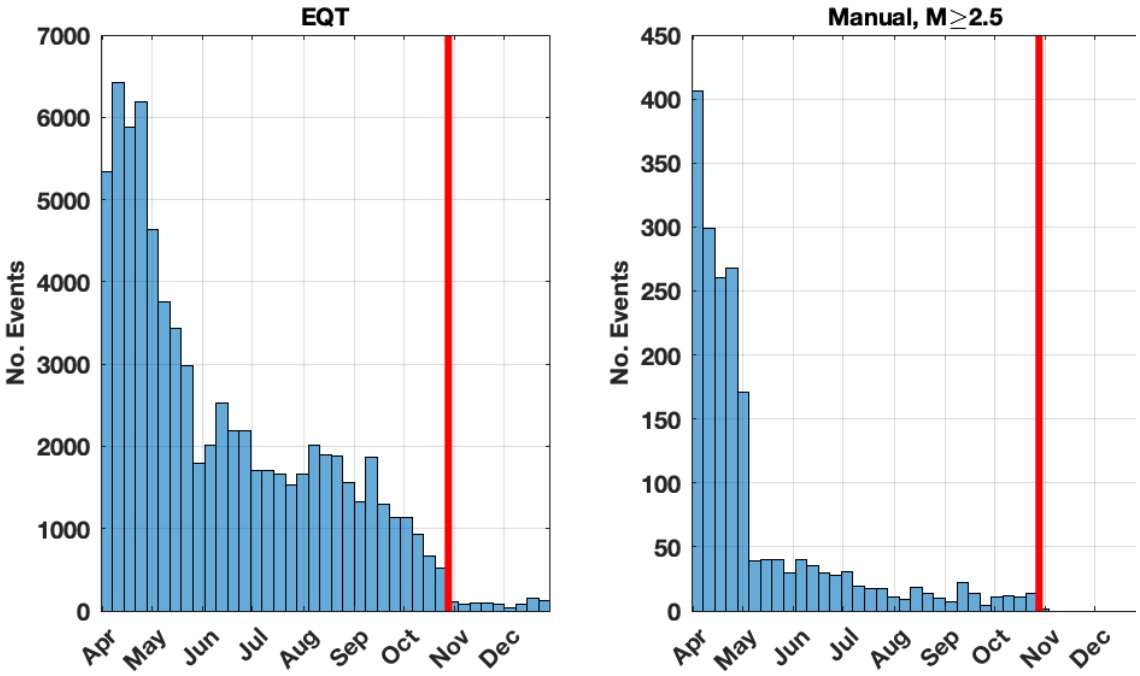

Figure 9. Histograms showing the total number of events detected by the manual

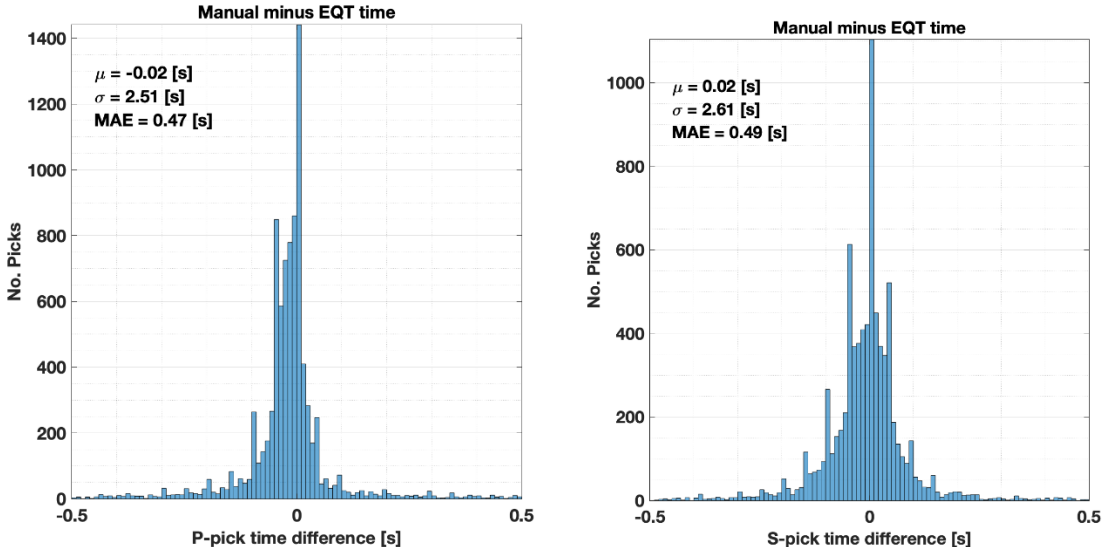

Figure 10. (left) The difference in P-wave arrival times for matching events found by the machine learning algorithm and events in the SEISAN catalog. (right) The difference in S-wave arrival times for matching events found by the machine learning algorithm and events in the SEISAN catalog.

Faulting Revealed by Aftershocks

Figures 7 and 8 reveal that aftershocks related to the Stanley earthquake align along mostly along a north-northwest trend. This linear trend lies mostly to the north of the mapped Sawooth normal fault (Crone et al., 2010). Moment tensor solutions from select events suggest both strike-slip and dip-slip motion (http://www.eas.slu.edu/eqc/eqc_mt/MECH.NA/2020.html). We suggest this aftershock pattern best represents a new, steeply-dipping, active strike-slip fault that we term the Stanley fault. Aftershocks also reveal a second east-trending band of seismicity that terminates to the west by the Stanley fault. This trend is similar to faults related to the Trans-Challis fault system and we suggest that the Stanley earthquake may have reactivated a relic fault related to Eocene and younger normal faulting. To date, we have no moment tensor solutions to better assess motion along this secondary fault. Radiation patterns will be assessed with our on-going analyses.

Summary

We developed two new aftershock catalogs for the March 31, 2020 M_w6.5 Stanley earthquake. We compare these catalogs to the USGS real-time catalog to show the improvements from the incorporation of a local seismic monitoring network. The first catalog relied on the same event picking approach as has been adopted by the USGS. These hand-picked phases were identified on our local XP seismic network to improve location and depth estimates. Our second catalog relied on the use of the EQTransformer deep learning approach to identify low signal-to-noise earthquakes that are related to low magnitude aftershocks. From the aftershock patterns, we identify two new active faults. Ongoing efforts using our new catalog will allow for improved aftershock magnitudes and robust moment tensor solutions to define the faults that moved, and how they moved, during the earthquake sequence. We will apply our machine learning approach to other regional earthquakes to improve seismic hazard assessments for Idaho.

References

Berti, C., Liberty, L., & Stachnik, J. (2020). *Aftershock deployment for Stanley, ID earthquake 2020* [Data set]. International Federation of Digital Seismograph Networks. https://doi.org/10.7914/SN/XP_2020.

Bockholt, B.M., Mikesell, T.D. and Liberty, L.M. (2021). Overview of Data Quality, Availability and Performance of the March 31, 2020 Stanley, Idaho Event Aftershock Deployment, presentation to the annual Seismological Society of America virtual meeting.

Bremner, P. M., Panning, M. P., Russo, R. M., Mocanu, V., Stanciu, A. C., Torpey, M., Hongsresawat, S., VanDecar, J. C., LaMaskin, T. A., & Foster, D. A. (2019). Crustal Shear Wave Velocity Structure of Central Idaho and Eastern Oregon From Ambient Seismic Noise: Results From the IDOR Project. *Journal of Geophysical Research: Solid Earth*, *124*(2), 1601–1625. https://doi.org/10.1029/2018JB016350

Crone, A.J., K. M. Haller, and R.S. Lewis, R.S., compilers (2010). Fault number 640, Sawtooth fault, in Quaternary fault and fold database of the United States: U.S. Geological Survey website, https://earthquakes.usgs.gov/hazards/qfaults, accessed 05/18/2020 01:19 PM

Davenport, K. K., J. A. Hole, B. Tikoff, R. M. Russo, and S. H. Harder (2017). A strong contrast in crustal architecture from accreted terranes to craton, constrained by controlled-source seismic data in Idaho and eastern Oregon, *Lithosphere* 9, no. 2, 325–340.

Havskov, J., Voss, P.H. and Ottemoller, L. (2020). Seismological Observatory Software: 30 Yr of SEISAN. *Seismological Research Letters*, 91 (3): 1846-1852. DOI: https://doi.org/10.1785/0220190313

Kennett B.L.N., E.R. Engdahl and R. Buland. 1995. "Constraints on seismic velocities in the earth from travel times" *Geophys. J. Int.* 122, 108–124. https://doi.org/10.1111/j.1365-246X.1995.tb03540.x

Klein, F. W. (2002). User's guide to HYPOINVERSE-2000, a Fortran program to solve for earthquake locations and magnitudes (No. 2002-171). US Geological Survey.

Liberty, L. M., Lifton, Z. M., & Dylan Mikesell, T. (2021). The 31 March 2020 Mw 6.5 Stanley, Idaho, earthquake: Seismotectonics and preliminary aftershock analysis. *Seismological Research Letters*, *92*(2), 663–678. https://doi.org/10.1785/0220200319

Liberty, L.M. and Mikesell, T.D. (2021). Aftershock monitoring of the M6.5 Stanley Earthquake, Final Technical Report; US Geological Survey Earthquake Hazards Program #G20AP00076, 7 p. (https://earthquake.usgs.gov/cfusion/external_grants/reports/G20AP00076.pdf) .

Mosher, S. G., & Audet, P. (2020). Automatic Detection and Location of Seismic Events From Time-Delay Projection Mapping and Neural Network Classification. *Journal of Geophysical Research: Solid Earth*, *125*(10), 1–18. https://doi.org/10.1029/2020JB019426

Mousavi, S.M., Ellsworth, W.L., Zhu, W. et al. (2020). Earthquake transformer—an attentive deep-learning model for simultaneous earthquake detection and phase picking. *Nat Commun* 11, 3952. https://doi.org/10.1038/s41467-020-17591-w

Pang, G., K. D. Koper, M. C. Stickney, J. C. Pechmann, R. Burlacu, K. L. Pankow, S. Payne, and H. M. Benz (2018). Seismicity in the Challis, Idaho, region, January 2014–May 2017: Late aftershocks of the 1983 MS 7.3 Borah Peak earthquake, *Seismol. Res. Lett.* 89, 1366–1378, doi: 10.1785/0220180058.

Pollitz, F. F., Hammond, W. C., & Wicks, C. W. (2021). Rupture process of the M 6.5 Stanley, Idaho, earthquake inferred from seismic waveform and geodetic data. *Seismological Society of America*, 92(2A), 699-709.

Stanciu, C., A., Russo, R. M., Mocanu, V. I., Bremner, P. M., Hongsresawat, S., Torpey, M. E. & Hole, J. A. (2016). Crustal structure beneath the Blue Mountains terranes and cratonic North America, eastern Oregon, and Idaho, from teleseismic receiver functions. *Journal of Geophysical Research: Solid Earth*, 121(7), 5049-5067.

U.S. Geological Survey 2020, Comprehensive Earthquake Catalog, accessed December 1, 2020, at: https://earthquake.usgs.gov/earthquakes/search/.

Waldhauser, F., & Ellsworth, W. L. (2000). A double-difference earthquake location algorithm: Method and application to the northern Hayward fault, California. Bulletin of the Seismological Society of America, 90(6), 1353-1368.

Wilbur, S., Liberty, L.M., Mikesell, T.D., Bockholt, B., and Johnson, J.B. (2021). Machine Learning Aftershock Detection for the Mw 6.5 March 31st, 2020 Stanley, Idaho Earthquake, abstract submitted to the annual meeting of the Seismological Society of America.

Yang, J., Zhu, H., Lay, T., Niu, Y., Ye, L., Lu, Z., et al. (2021). Multi-fault opposing-dip strike-slip and normal fault rupture during the 2020 M_w 6.5 Stanley, Idaho earthquake. *Geophysical Research Letters*, 48, e2021GL092510. https://doi.org/10.1029/2021GL092510